Green Chemistry

Accepted Manuscript

ROYAL SOCIETY OF CHEMISTRY

www.rsc.org/greenchem

Green Chemistry

COMMUNICATION

Carboxymethyl cellulose-templated synthesis of hierarchically structured metal oxides

Received 00th January 20xx,
Accepted 00th January 20xx

DOI: 10.1039/x0xx00000x

www.rsc.org/

Jong Wan Ko, Byung Il Lee, You Jung Chung and Chan Beum Park*

The synthesis of hierarchically structured metal oxides has been intensively pursued over many years for diverse industrial applications. Here, we report a simple but green approach for the synthesis of metal oxide fibers using carboxymethyl cellulose fibers (CMC). We synthesized 1D hierarchical metal oxides using CMC fibers as a sacrificial template. The electrostatic interaction between metal ions and carboxyl groups in CMC induced the formation of hierarchical structures of binary (e.g., CeO_2, ZnO) and tertiary (e.g., $CaMn_2O_4$) metal oxide fibers.

Cellulose, a main component of green plants, is the most abundant organic chemical on Earth, produced 10^{11} tons per year in the biosphere. The polysaccharide consists of D-glucose units linked by β-1,4-glycosidic bonds and has been widely utilized in diverse engineering fields because of its biocompatibility, abundance, and high chemical stability.[1] For example, metal oxides such as TiO_2, ZnO, and Al_2O_3 had been synthesized using cellulose as a sacrificial template through simple physical adsorption of precursor metal ions on the surface of cellulose matrix.[2] However, it was difficult to create hierarchically structured metal oxides having high crystallinity due to the limitation in controlling the interactions between precursor metal ions and cellulose template. While the synthesis of small particulate materials with distinguished structures and high specific surface area has been intensively studied in recent years,[3] the particles often exhibit a tendency to agglomerate, causing performance degradation during their applications.[4a] Hierarchically structured materials consisted of small particles with secondary structures can provide a facile pathway for efficient transfer of chemicals and electrons while maintaining active site area and unique physicochemical properties of the particles.[4]

Herein we report on the synthesis of hierarchically structured metal oxides made of nano-sized particles connected into 1D structure with high crystallinity using carboxymethyl cellulose (CMC) as a sacrificial template. CMC possesses negatively charged carboxyl groups and high loading capacity for metal ions, such as manganese, iron, and mercury, in aqueous media.[5] The cotton-like structure of CMC fibers can facilitate the formation of porous morphologies.[5] For examples, the synthesis of magnetic mesoporous carbon

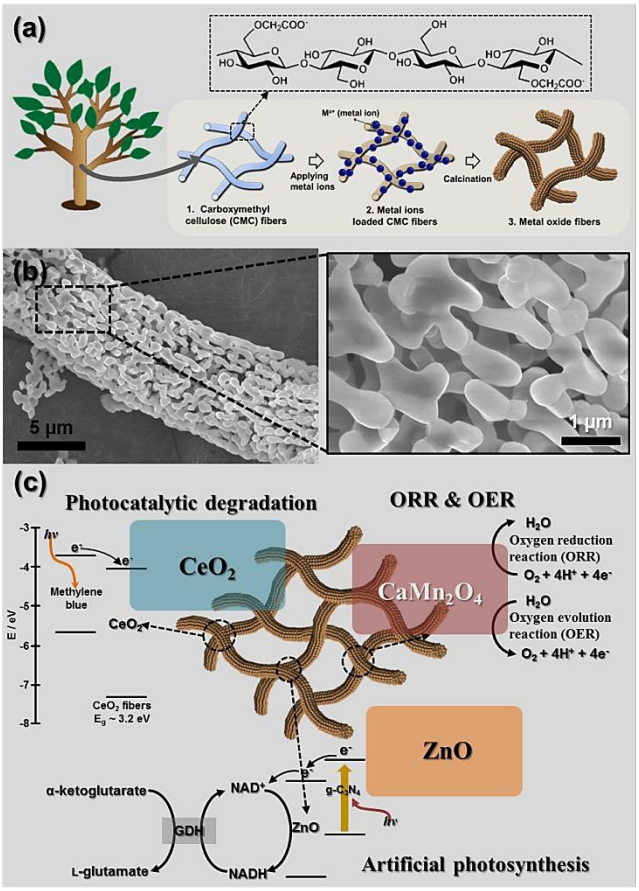

Scheme 1 (a) Schematic illustration of the synthetic process of hierarchical metal oxides using CMC fibers. (b) The SEM images of $CaMn_2O_4$ fiber with different magnification. (c) The applications of CeO_2 fibers for photocatalytic degradation of methylene blue, ZnO hybridized with g-C_3N_4 for photochemical NADH regeneration, and $CaMn_2O_4$ fibers as bi-functional electrocatalysts for oxygen reduction reaction (ORR) and oxygen evolution reaction (OER).

Department of Materials Science and Engineering, Korea Advanced Institute of Science and Technology (KAIST), 335 Science Road, Yuseong-gu, Daejeon 305-701, Republic of Korea.
E-mail: parkcb@kaist.ac.kr; Fax: +82 42 350 3310; Tel: +82 42 350 3340
† Electronic Supplementary Information (ESI) available: Experimental details and supporting data of SEM, TEM, XRD, EDX, TGA, Zeta potential measurement, FT-IR spectra, and UV-visible spectra. See DOI: 10.1039/x0xx00000x

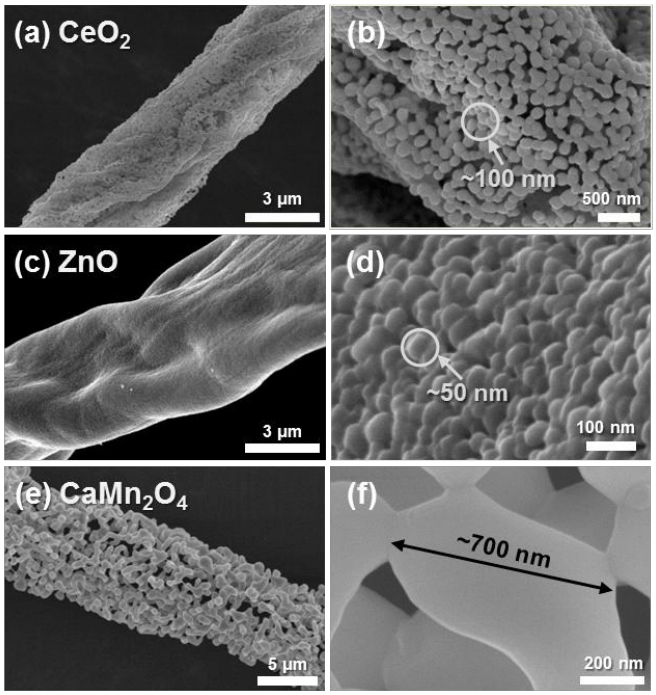

Figure 1 SEM images of (a, b) CeO_2, (c, d) ZnO, and (e, f) $CaMn_2O_4$ with different magnification.

composites have reported using CMC.[6] Furthermore, CMC is a cost-effective material with good chemical stability, suitable for industrial-scale applications. We have synthesized hierarchical binary (e.g., CeO_2, ZnO) and ternary metal oxides (e.g., $CaMn_2O_4$) using CMC fibers according to the steps illustrated in **Scheme 1a**. Briefly, we incubated CMC fibers in a metal precursor solution to obtain metal ion-loaded CMC fibers through electrostatic interaction between the carboxyl groups in CMC fibers and the metal ions in the solution. Hierarchical metal oxide fibers shown in **Scheme 1b** were created through the calcination of the metal ion-loaded CMC fibers under air atmosphere. The synthesized metal oxide (i.e., CeO_2) also showed amendable structure and macroscopic porous structure that can show low specific gravity (0.316 g cm^{-3}) (**Figure S1**). According to our analysis, the resulting hierarchically structured metal oxides and distinguish surface properties (i.e., valence of metal ions) from conventional metal oxides exhibited high catalytic performances towards organic pollutant degradation, artificial photosynthesis, and oxygen reduction/evolution (**Scheme 1c**).

CMC fibers preferentially bind to divalent metal ions because they contain numerous hydroxyl and carboxyl groups that can chelate metal ions.[7] We considered that such property of CMC fibers could restrain particle growth during calcination process and that an appropriate control of synthetic conditions would enable the fabrication of 1D hierarchical metal oxides. To verify the existence of Ce^{3+} ions in CMC fibers after immersion in $CeCl_2$ solution, we conducted energy dispersive X-ray spectroscopy, zeta potential, inductively coupled plasma (ICP), and FT-IR analysis. As shown in **Figure S2**, X-ray absorption peaks corresponding to Ce element were observed in the Ce^{3+}-adopted CMC fibers, while SEM images exhibited no difference between pristine CMC fibers and Ce^{3+}-CMC fibers. To investigate possible electrostatic interaction between Ce^{3+} ions and carboxyl groups in CMC fibers, we analyzed the change of the surface charge of CMC fibers using zeta potential and ICP measurement after the loading of different amounts of Ce^{3+} ions. A suspension of pristine CMC fibers exhibited a zeta potential of approximately -4.76 that originated from the carboxyl groups (**Figure S3**). The value of the negative charge decreased with the increment of bound Ce^{3+} ions to the CMC fibers due to the higher number of Ce^{3+} ions bound to carboxyl groups. Cation-loading capacity of CMC fiber is known to be 1.08 meq g^{-1},[5d] which corresponds to 360 μmole of Ce^{3+} ions per gram. In this work, the amount of adsorbed Ce^{3+} ions to CMC fibers was saturated to 350 μmole of Ce^{3+} ions g^{-1}, indicating that Ce^{3+} ions were almost fully bound to CMC fibers through electrostatic interactions. To verify the interaction between carboxyl groups and Ce^{3+} ions, we further conducted FT-IR analysis. **Figure S4a** shows FT-IR absorption peaks corresponding to the stretching vibration modes of hydroxyl groups and carboxyl groups.[8] The hydroxyl group stretching band shifted from 3450 cm^{-1} for pristine CMC fibers to 3409 cm^{-1} for Ce^{3+}-CMC fibers. This shift implies an increased intermolecular hydrogen bonding between metal ions and hydroxyl groups on the surface of CMC fibers.[8] The FT-IR spectra show the difference in the symmetric

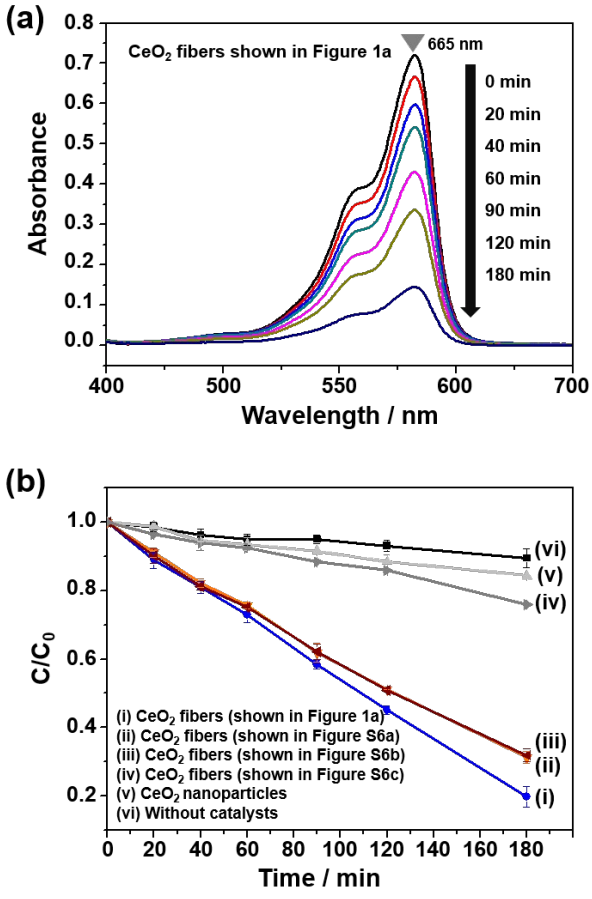

Figure 2 (a) UV-visible spectra of MB solution monitored in the presence of CeO_2 fibers (shown in Figure 1a) during visible light irradiation (λ > 420 nm). (b) Time profiles of MB photodegradation with (i-iv) CeO_2 fibers, (v) CeO_2 nanoparticles, and (vi) without catalyst under visible light irradiation. The change of MB concentration (C/C_0) was estimated from the intensity decrease of the absorbance at 665 nm. The error bars in the spectra represent the standard deviations of three independent measurements for each data point.

vibrational mode of carboxyl groups in CMC fibers (1415 cm^{-1}) and Ce^{3+}-CMC fibers (1324 cm^{-1}), indicating direct interaction between Ce^{3+} ions and the carboxyl groups in CMC fibers. We also modified the surface properties of CMC (i.e., the extent of ionization of carboxyl groups) by protonation/deprotonation of the carboxyl groups. The FT-IR spectra are presented with peak locations and assignments (**Figure S4b**). At acidic condition (0.1 M HCl), the carboxyl groups on CMC were fully protonated. The carbonyl stretch[9] of carboxylic acid groups was observed at 1732 cm^{-1}. The FT-IR spectrum of basic treated CMC (1 M NaOH) is different from that at low pH. The carboxyl groups were deprotonated, as shown by the absence of carbonyl stretch[9] at 1732 cm^{-1} and the appearance of $–COO^-$ asymmetric stretch[9] at 1596 cm^{-1}. As shown in **Figure S5a** and **b**, the morphologies of CeO_2 from HCl treated CMC could not be controlled due to lower extent of deprotonated carboxyl groups. Based on high metal ion affinity of deprotonated carboxyl groups ($–COO^-$) in CMC, different morphologies of CeO_2 fibers were obtained by changing precursor concentration (**Figure S5c** and **d**).

We investigated the decomposition of CMC fibers and the formation of CeO_2 fibers during the calcination process. According to thermogravimetric analysis (TGA) and differential scanning calorimetry (DSC) analysis, Ce^{3+}-CMC fibers started to decompose at around 240 °C with the exothermal peak corresponding to the decomposition of cellulose at 330 °C (**Figure S6a**). The small endothermic peak at around 350 °C indicates the oxidation of Ce^{3+} ions to form CeO_2. The decomposition of residual cellulose matrix was observed with the additional exothermal peak at over 370 °C. This result suggests that CeO_2 phase was formed before full decomposition of CMC fibers. Thus, CeO_2 fibers could retain the unique structure that consisted of interconnected nanospheres with numerous pores. The morphology of hierarchical CeO_2 fibers was significantly affected by precursor concentration and calcination temperature. According to our observation, the CeO_2 fibers having 1D hierarchical structures consisted of numerous nanospheres (~100 nm) (**Figures 1a, b**) were synthesized with 4 mM $CeCl_3$ followed by calcination at 800 °C. As shown in **Figure S6b**, pore sizes in the CeO_2 fibers were distributed mostly in the range of mesopores (2-50 nm) and macropores (larger than 50 nm). Our XRD analysis confirmed the formation of a highly crystalline phase of CeO_2 by showing the corresponding X-ray diffraction pattern of CeO_2 (PDF# 43-1002) (**Figure S7a**). At lower concentration of Ce^{3+} ions (1 mM), CeO_2 fibers exhibited lower connectivity between larger CeO_2 nanoparticles (~180 nm) due to the decreased amount of Ce^{3+} ions (81.8 µmole g^{-1} according to ICP analysis) adsorbed in the CMC fibers (**Figure S8a**). When calcination was conducted at an elevated temperature of 1000 °C, individual CeO_2 particles became larger (~300 nm) than those of CeO_2 fibers calcinated at 800 °C (**Figure S8b**) due to the thermodynamic facilitation of particle growth at high temperature. Much denser CeO_2 fibers with pores on the smooth surface were obtained at higher Ce^{3+} ion concentration (20 mM) (**Figure S8c**). The type of metal elements also influenced the resulting structure of metal oxides; while ZnO fibers also consisted of spherical, crystalline ZnO nanoparticles (~50 nm) and numerous pores (< 10 nm) (**Figures 1c, d,** and **Figure S7b**), they exhibited a pleated surface and denser 1D structure than that of CeO_2 fibers (**Figures 2c, d**). $CaMn_2O_4$, a ternary metal oxide, had submicron-sized granules (~700 nm) of a highly crystalline phase of $CaMn_2O_4$ (PDF# 70-4889) connected into fibers (**Figures 1e, f,** and **Figure S7c**). The void and particle size in the $CaMn_2O_4$ fibers varied depending on the amount of CMC fibers in the precursor solution (**Figures S9a**, **b**). With a higher amount of CMC fibers (120 mg mL^{-1}), $CaMn_2O_4$ particles were readily formed with approximate size of 700 nm due to the insufficiency of ion concentration (Ca 10.3 µmole g^{-1}; Mn 22.8 µmole g^{-1}) in CMC fibers for the formation of fibrous $CaMn_2O_4$ (**Figure S9c**). This result indicates that the density of adopted metal ions in CMC fibers influences the final morphology of $CaMn_2O_4$, similar to the formation of CeO_2 fibers.

We investigated catalytic activities of thus-synthesized hierarchical metal oxides for photocatalysis, artificial photosynthesis, and electrocatalysis. We evaluated the activity of hierarchically structured CeO_2 fibers by measuring photocatalytic

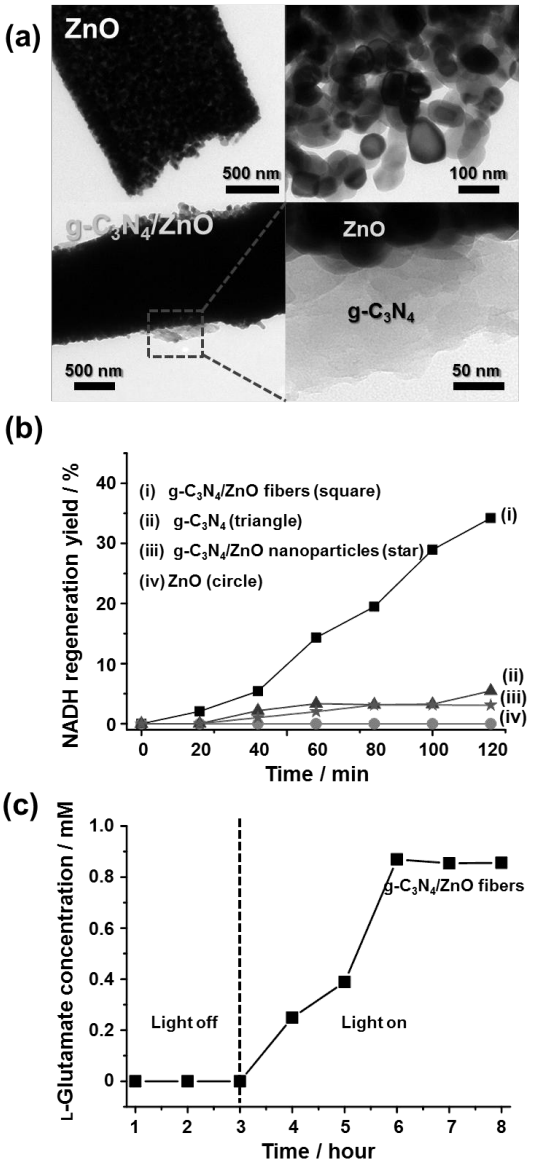

Figure 3 (a) TEM images of ZnO fiber and g-C_3N_4/ZnO composite fiber with different magnification. (b) Photochemical NADH regeneration of g-C_3N_4/ZnO fibers, g-C_3N_4, g-C_3N_4/ZnO nanoparticles, and ZnO fibers under visible light irradiation (λ > 420 nm). (c) Photoenzymatic conversion of α-ketoglutamate to L-glutamate with g-C_3N_4/ZnO composite was conducted after 3 hour of the dark reaction in NADH regeneration.

degradation of methylene blue (MB). **Figure 2a** shows the change of UV-visible absorption spectrum of MB in the presence of CeO_2 fibers shown in **Figure 1a** under visible light (λ > 420 nm). The absorption peak continued to decline with visible light illumination, and approximately 80% of MB was degraded within 3 hours. To compare the rate of MB degradation with that by CeO_2 nanoparticles (< 25 nm, BET surface area 34.16 $m^2 g^{-1}$) (**Figures S10, S11**), we plotted the time profiles of normalized concentration (C/C_0) change from the normalized absorbance (A/A_0) at 665 nm (**Figure 2b**). Despite of the smaller specific surface area of CeO_2 fibers (0.24 ~ 3.17 $m^2 g^{-1}$) than that of CeO_2 nanoparticles (34.16 $m^2 g^{-1}$), CeO_2 fibers showed much enhanced photocatalytic activity than CeO_2 nanoparticles. The highest value of rate constant (k) for MB degradation by the CeO_2 fibers was calculated to be 1.05×10^{-2} min^{-1}, which was 20-fold higher than that by CeO_2 nanoparticles (k = 0.046×10^{-2} min^{-1}). In the photodegradation of MB molecules, photo-excited electrons at the LUMO level of MB (-3.60 V)[10] needs to be transferred to the conduction band of CeO_2 (-4.06 V)[11]. The oxidative forms of MB then become a cationic radical that takes part in the self-degradation. Moreover, CeO_2 catalytically reduce oxygen to reactive oxygen species (i.e., hydroxyl radical) which can oxidize and decolorize MB molecules.[12] The Catalytic activity for hydroxyl radical generation can be significantly increased by higher concentration of Ce^{3+} ions on CeO_2 surface.[13] X-ray photoelectron spectroscopy (XPS) analysis was conducted in order to characterize the valence state of cerium in CeO_2 samples. For Ce 3d XPS spectrum of CeO_2 fibers, the ratio of peaks corresponding to the Ce^{3+} state (885.2 and 902.2 eV) is higher than those of CeO_2 nanoparticles (10.4 mol% for CeO_2 fibers; 4.8 mol% for CeO_2 nanoparticles) (**Figure S12**). The improved photocatalytic performance of CMC-templated CeO_2 fibers should stem from the high concentration of Ce^{3+} ions by producing reactive oxygen species (e.g., hydroxyl radical), which could degrade MB molecules. We determined the hydroxyl radical ($OH^{\cdot}$), which could accelerate MB degradation reaction, by measuring the fluorescent 2-hydroxyl terephthalate (TA-$OH^{\cdot}$) using a fluorescence spectroscopy. As shown in **Figure S13**, the photoluminescence intensity of TA-$OH^{\cdot}$ at 425 nm increased during photocatalytic MB degradation with CeO_2 fibers, while TA-$OH^{\cdot}$ was not observed with CeO_2 nanoparticles (**Figure S13 inset**).

Recently, ZnO had been extensively studied for solar energy harvesting due to high electronic mobility with a good chemical stability.[14] We analyzed light harvesting capability of the 1D hierarchical ZnO fibers toward biocatalyzed artificial photosynthesis that aims visible light-driven regeneration of NAD(P)H coupled with redox enzymatic reaction.[15] Since ZnO has a large bandgap (3.1 eV) to absorb mostly UV light, we utilized graphitic carbon nitride (g-C_3N_4) as a visible light-active material (**Figure S14**). The composite of g-C_3N_4 sheets and ZnO fibers (g-C_3N_4/ZnO fibers) was prepared by simple mixing and evaporation method (**Figure 3a** and **Figure S15**). As illustrated in **Figure S16**, g-C_3N_4 can absorb visible light and generate electrons in its conduction band (-1.12 V vs NHE),[16] and photo-excited electrons are transferred to ZnO fibers due to the more positive position of the conduction band edge of ZnO compared to g-C_3N_4 (at least 0.4 V more positive), thereby regenerating NADH in conjunction with redox enzymatic synthesis of L-glutamate from α-ketoglutarate. The NADH regeneration rate by g-C_3N_4/ZnO fibers was 5.25 μmole g^{-1} $hour^{-1}$, which was eight times higher than that of g-C_3N_4/ZnO nanoparticles (0.63 μmole g^{-1} $hour^{-1}$) (**Figure 3b**). We attribute the increased NADH regeneration rate of g-C_3N_4/ZnO fibers to the hierarchical morphology that provides facile electron transfer between g-C_3N_4 and ZnO fibers. As shown in **Figure S17**, in the case of g-C_3N_4/ZnO fibers, higher photocurrent response than those of bare g-C_3N_4 and g-C_3N_4/ZnO nanoparticles was observed, which means that superior photo-activity of g-C_3N_4/ZnO fibers under visible light irradiation. By coupling NADH photoregeneration with redox enzymatic reaction of L-glutamate dehydrogenase (GDH), L-glutamate was successfully produced under visible light (**Figure 3c**).

We found that the hierarchical $CaMn_2O_4$ fibers have high potential for electrocatalytic applications of oxygen reduction (ORR) and evolution reactions (OER). Manganese-based oxides have been widely studied for energy storage and catalysis due to the advantages of cost efficiency, high abundance, and low toxicity.[1] We examined electrocatalytic activity of $CaMn_2O_4$ fibers for bi functional reactions of ORR and OER. We considered that the distinctive structure of hierarchical $CaMn_2O_4$ fiber would prevent crystalline $CaMn_2O_4$ particles from agglomeration that can inhibit electrochemical performance. As a control, we prepared bulk $CaMn_2O_4$ by a conventional hydrothermal process (**Figure S18**). When we analyzed electrocatalytic activities of $CaMn_2O_4$ for ORR

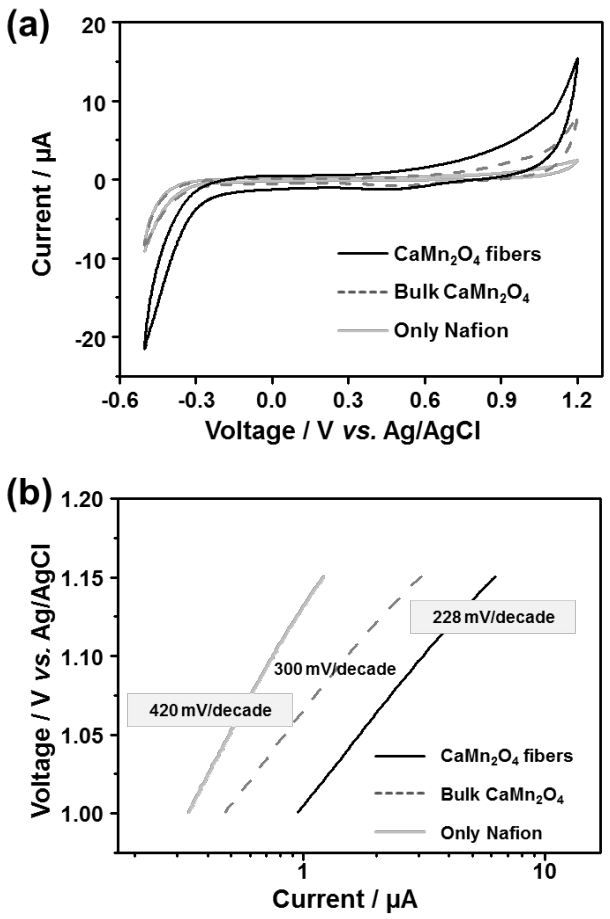

Figure 4 (a) Cyclic voltammetry curves of $CaMn_2O_4$ fibers (black solid line), bulk $CaMn_2O_4$ (grey dash line), and only Nafion (grey solid line) in 0.1 M phosphate buffer solution (pH 7.0) saturated with O_2. (b) The plots of Tafel slope of OER current in (b).

and OER using cyclic voltammetry (CV), cathodic current of $CaMn_2O_4$ fibers was observed at -0.327 V (**Figure 4a**), which was much lower than those of bulk $CaMn_2O_4$ (-0.443 V) and Nafion-coated glassy carbon (-0.449 V) electrodes. The cathodic current of $CaMn_2O_4$ fibers indicates a facile electrocatalytic reaction of O_2 reduction in aqueous media. In the oxidation range of cyclic voltammetric analysis, the $CaMn_2O_4$ fiber electrode showed an anodic current of 5 μA at a lower overpotential (0.349 V) than that of bulk $CaMn_2O_4$ (0.512 V). The hierarchical $CaMn_2O_4$ fibers exhibited much smaller Tafel slope decrease (228 mV/decade) than that (300 mV/decade) of bulk $CaMn_2O_4$ (**Figure 4b**). The smaller Tafel slope of $CaMn_2O_4$ fibers indicates faster electron transfer during OER. Although Ca is considered to be inactive in redox reaction such as ORR and OER.[18] In photosystem II (PS II) oxygen evolution center, Ca is considered as a critical cofactor for the OER, as providing and an active and binding site for oxygen-containing species.[18] For this reason, we analyzed the state of Ca in $CaMn_2O_4$ samples using XPS. (**Figure S19**) In the case of $CaMn_2O_4$ fibers, typical Ca 2p peak (346.5 eV) and lower binding energy peak (345.1 eV) are observed, while similar spectra of Mn 2p were obtained from both $CaMn_2O_4$ samples. The difference in Ca 2p state, which correlated with the shift of O1s peak toward lower binding energy (from 529.7 to 529.0 eV), could affect behaviors (i.e., attachment and activation) of oxygen species[19] and would facilitate the ORR and OER reaction of $CaMn_2O_4$ fibers. In addition, the enhanced bi-functional electrocatalytic performance of $CaMn_2O_4$ fibers is also attributed to their hierarchical structure that enables facile mass transfer for ORR and OER. Our results show bi-functional electrocatalytic activity of the $CaMn_2O_4$ fibers, unlike bulk $CaMn_2O_4$; electrocatalytic OER activity of $CaMn_2O_4$ is reported for the first time in this work.

Conclusions

Metal oxides have attracted high attention in the past decades due to their distinct photocatalytic and electrical activities with high chemical, thermal, and mechanical stabilities. In this work, we have demonstrated the utility of CMC fibers as a sacrificial template to produce binary and tertiary metal oxides fibers. The electrostatic interaction between metal ions and the carboxyl groups in CMC fibers induced a hierarchical structure of metal oxides. The morphologies of synthesized metal oxides (e.g., CeO_2, ZnO, and $CaMn_2O_4$) could be controlled according to synthetic conditions, such as metal precursor concentration, calcination temperature, and the amount of CMC fibers. Thus-synthesized CMC-templated metal oxide fibers exhibited enhanced performances for photocatalytic, photochemical, and electrocatalytic reactions. The CeO_2 fibers showed much higher photocatalytic activity than CeO_2 nanoparticles due to superior ability to generate reactive oxygen species which can degrade organic pollutants. We also demonstrated that hierarchical ZnO fibers hybridized with g-C_3N_4 could provide directional charge transfer pathway and showed their utility for biocatalyzed artificial photosynthesis through visible light-driven chemical NADH regeneration coupled with redox enzymatic reaction. The electrochemical properties of $CaMn_2O_4$ fibers enabled bi-functional reactions of ORR and OER. We expect that the economical and environmentally friend approach could be extended to green synthesis of hierarchically structured materials of other metal oxides.

Acknowledgements

This study was supported by grants from the National Research Foundation (NRF) via the National Leading Research Laboratory (NRF-2013R1A2A1A05005468) and the Intelligent Synthetic Biology Center of Global Frontier R&D Project (2011-0031957), Republic of Korea.

Notes and references

1 (a) R. J. Moon, A. Martini, J. Nairn, J. Simonsen and J. Youngblood, *Chem. Soc. Rev.* 2011, **40**, 3941; (b) I. Delidovich, K. Leonhard and R. Palkovits, *Energy Environ. Sci.* 2014, **7**, 2803; (c) A. S. Amarasekara and O. S. Owereh, *Ind. Eng. Chem. Res.* 2009, **48**, 10152; (d) P. Laaksonen, A. Walther, J. M. Malho, M. Kainlauri, O. Ikkala and M. B. Linder, *Angew. Chem. Int. Ed.* 2011, **50**, 8688.
2 (a) J. Huang and Y. Gu, *Curr. Opin. Colloid Interface Sci.* 2011, **16**, 470; (b) E. Ghadiri, N. Taghavinia, S. M. Zakeeruddin, M. Gratzel and J.-E. Moser, *Nano Lett.* 2010, **10**, 1632; (c) J. T. Korhonen, P. Hiekkataipale, J. Malm, M. Karppinen, O. Ikkala and R. H. A. Ras, *ACS Nano* 2011, **5**, 1967.
3 (a) M. Gu, I. Belharouak, A. Genc, Z. Wang, D. Wang, K. Amine, F. Gao, G. Zhou, S. Thevuthasan, D. R. Baer, J. G. Zhang, N. D. Browning, J. Liu and C. Wang, *Nano Lett.* 2012, **12**, 5186; (b) C. He, A. J. Grutter, M. Gu, N. D. Browning, Y. Takamura, B. J. Kirby, J. A. Borchers, J. W. Kim, M. R. Fitzsimmons, X. Zhai, V. V. Mehta, F. J. Wong and Y. Suzuki, *Phys. Rev. Lett.* 2012, **109**, 197202.
4 (a) Y. Ren, Z. Ma and P. G. Bruce, *Chem. Soc. Rev.* 2012, **41**, 4909; (b) A. Q. Pan, H. B. Wu, L. Zhang and X. W. Lou, *Energy Environ. Sci.* 2013, **6**, 1476.
5 (a) J. D. Reid, G. C. Daul, *Text. Res. J.* 1949, **19**, 794; (b) A. B. Bourlinos, D. Petridis, *Chem. Commun.* 2002, 2788; (c) Y. Gong, Y. Liu, Z. Xiong, D. Zhao, *Environ. Sci. Technol.* 2014, **48**, 3986; (d) S. Yang, S. Fu, H. Liu, Y. Zhou, X. Li, *J. Appl. Polym. Sci.* 2010, **119**, 1204; (e) Y. Zhang, Y. Liu, X. Wang, Z. Sun, J. Ma, T. Wu, F. Xing, J. Gao, *Carbohydr. Polym.* 2014, **101**, 392.
6 (a) Q. Wu, W. Li, J. Tan, X. Nan, S. Liu, *Appl. Surf. Sci.* 2015, **332**, 354; (b) Q. Wu, W. Li, J. Tan, S. Liu, *RSC Adv.* 2014, **4**, 61518; (c) D. Yamaguchi, K. Furukawa, M. Takasuga, K. Watanabe, *Sci. Rep.* 2014, **4**, 6053.
7 (a) X. Zhao, L. Lv, B. Pan, W. Zhang, S. Zhang and Q. Zhang, *Chem. Eng. J.* 2011, **170**, 381; (b) J. Wang, X. Lin, X. Luo and Y. Long, *Chem. Eng. J.* 2014, **252**, 415; (c) N. C. Cady, J. L. Behnke and A. D. Strickland, *Adv. Funct. Mater.* 2011, **21**, 2506.
8 F. He, D. Zhao, J. Liu and C. B. Roberts, *Ind. Eng. Chem. Res.* 2006, **46**, 29.
9 L. T. Cuba-Chiem, L. Huynh, J. Ralston and D. A. Beattie, *Langmuir* 2008, **24**, 8036.
10 J. S. Lee, K. H. You and C. B. Park, *Adv. Mater.* 2012, **24**, 1084.
11 J. W. Ko, J. H. Kim and C. B. Park, *J. Mater. Chem. A* 2013, **1**, 241.
12 D. Channei, B. Inceesungvorn, N. Wetchakun, S. Ukritnukun, A. Nattestad, J. Chen and S. Phanichphant, *SCi. Rep.* 2014, **4**, 5757.
13 C. T. Campbell and C. H. F. Peden, *Science* 2005, **309**, 713.
14 Q. Zhang, C. S. Dandeneau, X. Zhou and C. Cao, *Adv. Mater.* 2009, **21**, 4087.
15 (a) S. H. Lee, J. H. Kim and C. B. Park, *Chem. Eur. J.* 2013, **19**, 4392; (b) J. H. Kim, D. H. Nam and C. B. Park, *Curr. Opin.*

Biotechnol. 2014, **28**, 1; (c) J. Ryu, S. H. Lee, D. H. Nam and C. B. Park, *Adv. Mater.* 2012, **24**, 1084; (d) J. Ryu, D. H. Nam, S. H. Lee and C. B. Park, *Chem. Eur. J.* 2014, **20**, 12020; (e) S. H. Lee, D. H. Nam, J. H. Kim, J-O. Baeg and C. B. Park, *ChemBioChem* 2009, **10**, 1621; (f) J. H. Kim, M. Lee and C. B. Park, *Angew. Chem. Int. Ed.* 2014, **53**, 6364; (g) J. H. Kim, M. Lee, J. S. Lee and C. B. Park, *Angew. Chem. Int. Ed.* 2012, **51**, 517; (h) M. Lee, J. U. Kim, J. S. Lee, B. I. Lee, J. Shin and C. B. Park, *Adv. Mater.* 2014, **26**, 4463.

16 Y. Wang, R. Shi, J. Lin and Y. Zhu, *Energy Environ. Sci.* 2011, **4**, 2922.

17 (a) Y. Liang, H. Wang, J. Zhou, Y. Li, J. Wang, T. Regier and H. Dai, *J. Am. Chem. Soc.* 2012, **134**, 3517; (b) F. Cheng, J. Shen, B. Peng, Y. Pan, Z. Tao and J. Chen, *Nat. Chem.* 2011, **3**, 79; (c) Y.-K. Sun, M.-J. Lee, C. Yoon, J. Hassoun, K. Amine and B Scrosati, *Adv. Mater.* 2012, **24**, 1192; (d) Y. Cao, L. Xiao, W. Wang, D. Choi, Z. Nie, J. Yu, L. Saraf, Z. Yang and J. Liu, *Adv. Mater.* 2011, **23**, 3155.

18 (a) X. Han, T. Zhang, J. Du, F. Cheng, J. Chen, *Chem. Sci.* 2013, **4**, 368; (b) C. F. Yocum, *Coord. Chem. Rev.* 2008, **252**, 296.

19 M. Wiechen, I. Zaharieva, H. Dau, P. Kurz, *Chem. Sci.* 2012, **3**, 2330.

Green Chemistry

COMMUNICATION

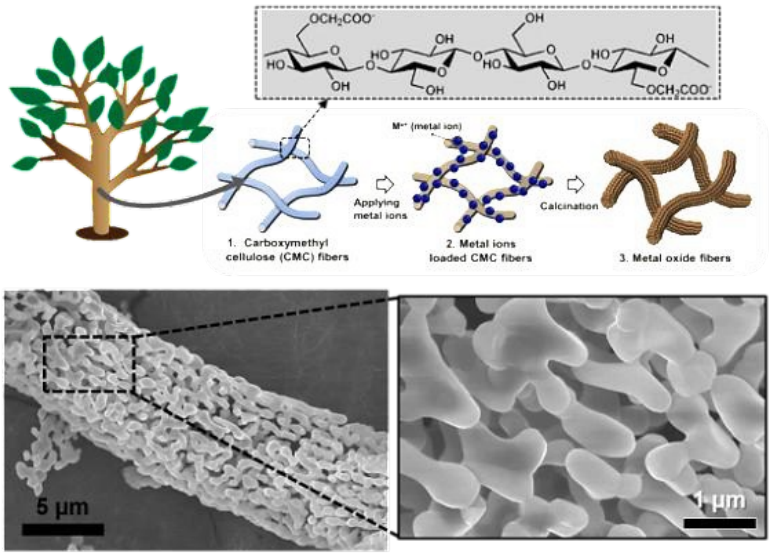

Cellulose-templated synthesis: Porous metal oxides were successfully synthesized through a simple and environmentally friendly process using carboxymethyl cellulose (CMC) fibers as a sacrificial template.

Electronic Supplementary Information

Carboxymethyl cellulose-templated synthesis of hierarchically structured metal oxides

*Jong Wan Ko, Byung Il Lee, You Jung Chung, Chan Beum Park**
Department of Materials Science and Engineering, Korea Advanced Institute of Science and Technology (KAIST), 335 Science Road, Daejeon 305-701, Republic of Korea

Experimental Details

Materials: $CeCl_3 \cdot 7H_2O$ (trace metal basis, 99.9%), $Ca(NO_3)_2 \cdot 4H_2O$ (99.0%), $Mn(NO_3)_2 \cdot 4H_2O$ (purum p.a., > 97.0%), carboxymethyl cellulose (fibers), ZnO nanoparticles (< 50 nm), and other reagents were purchased from Sigma-Aldrich (St. Louis, USA) and used without purification.

Preparation of CeO_2 fibers: For synthesis of CeO_2 fibers, 2 g of carboxymethyl cellulose (CMC) was immersed in 50 ml of different concentrations of $CeCl_3 \cdot 7H_2O$ solution (1 ~ 4 mM). After 30 minutes of incubation under ambient condition, CMC was separated, washed with deionized water, and calcinated at different temperatures (800 ~ 1000 ℃) for 2 hours.

Synthesis of ZnO fibers: ZnO fibers was prepared 5 g of CMC and 50 ml of $Zn(NO_3)_2 \cdot 6H_2O$ solution (0.2 mM). Mixture solution was incubated under ambient condition for 30 minutes. The CMC was separated, washed with deionized water and calcinated at 500 ℃ for 2 hours.

Preparation of $CaMn_2O_4$ fibers: $CaMn_2O_4$ fibers were prepared with a different amount of CMC (0.05 ~ 4 g) and a solution of 40 ml of $Ca(NO)_3 \cdot 4H_2O$ (25 mM) and $Mn(NO)_3 \cdot 4H_2O$ (62.5 mM). $CaMn_2O_4$ fibers were obtained by calcinating CMC at 1000 ℃ under air atmosphere for 2 hours.

Synthesis of g-C_3N_4 powder: g-C_3N_4 was prepared according to the previous literature. Briefly, 3 g of dicyandiamide in alumina crucible was calcinated at 600 ℃ under air for 4 hours.

Characterization: The morphologies of each sample were observed using a S-4800 field emission scanning electron microscopy (Hitachi Co., Japan) at an electron acceleration voltage of 5 ~ 10 kV. The X-ray diffraction patterns were recorded using a D/MAX-RB X-ray diffractometer (Rigaku Co., Japan) with a scan rate of 4 °/min, range of 10 °~ 70 °, and a Cu Kα radiation wavelength of 1.5418 Å. Absorbance spectra were obtained using a UV-visible spectrophotometer (Jasco Inc., Japan) with a diffuse-reflectance mode. The mass change as a function of temperature in the isothermal mode was measured using a Setsys 16/18 thermal analyzer (Setaram, France) with a heating rate of 10 ℃/min and a temperature range of 25 ~ 800 ℃ under air. The surface charges of Ce^{3+}-CMC fibers dispersion in deionized water at pH 7.0 were investigated by zeta-potential measurements using a Zetasizer nano zs (Malvern, UK). The FT-IR spectra of Ce^{3+}-CMC fibers, HCl and NaOH treated CMC fibers were obtained using a FT-IR 200 spectrophotometer (Jasco Inc., Japan). The amount of adsorbed metal ions in CMC fibers was measured using an Agilent ICP-MS 7700S inductively coupled with a plasma mass spectrometer (Agilent, USA). A spectrofluorometric study was conducted using an RF-5301PC (Shimadzu Co., Japan) with an excitation wavelength of 320 nm. X-ray photoelectron spectroscopic analysis was carried out using a K-alpha (Thermo VG Scientific, UK) in the range of 0 – 1300 eV. We measured pore size and surface area of CeO_2 fibers by Brunauer-Emmett-Teller (BET) method using ASAP 2020 N_2 gas sorption analyzer (Micromeritics, USA).

Methylene blue (MB) degradation test: A reactive solution was prepared by mixing 30 mg of CeO_2 samples (CeO_2 fibers and bulk CeO_2) in a 30 mL of MB solution (26.7 μM). The reactive solution was incubated and stabilized in the dark for 4 hours with vigorous stirring to complete the equilibrium of adsorption-desorption of MB molecules on the surface of CeO_2 samples before visible light irradiation. The solution was irradiated by a xenon lamp (450 W)

with a 420 nm cut-off filter. To analyze the degree of MB degradation, the absorbance of the reaction solution at 665 nm was measured after removing CeO_2 samples by centrifugation.

Preparation of g-C_3N_4/ZnO nanoparticle and g-C_3N_4/ZnO fiber: Hybridization of g-C_3N_4 and ZnO was carried out with different amount of g-C_3N_4. g-C_3N_4 were dispersed in DI water by sonication (20 mg in 50 ml). ZnO was also dispersed in DI water (100 mg in 10 ml), and different amounts of g-C_3N_4 (1, 3, 5, and 10 wt% of g-C_3N_4) were added to the ZnO dispersed aqueous solution. The mixture solution was incubated at 70 ℃ for overnight to evaporate DI water. We conducted photochemical NADH regeneration with different g-C_3N_4/ZnO nanoparticles (fibers) (1, 3, 5, and 10 wt%), and figured out the optimized g-C_3N_4 content (3 wt%) (data not shown).

Photochemical nicotineamide adenine dinucleotide (NADH) regeneration and photoenzymatic synthesis of L-glutamate: The photochemical regeneration of NADH was conducted visible light irradiation with a xenon lamp (450 W) at room temperature. The reaction solution was prepared by dissolving 1 mM of NAD^+ and 250 μM of $[Cp^*Rh(bpy)H_2O]^{2+}$ (**M**) in 3 mL of phosphate buffer (100 mM, pH 7.0) containing 15 w% triethanolamine. ZnO fiber (100 mg), g-C_3N_4/ZnO nanoparticles (100 mg), g-C_3N_4 powder (3 mg), and g-C_3N_4/ZnO fibers (100 mg) were dispersed in the reactive solution. The concentration of NADH in reactive solution was measured by analyzing its absorbance at 340 nm using UV-visible spectrophotometer (Jasco Inc., Japan). For the photoenzymatic synthesis of L-glutamate was coupled with photoregeneration of NADH using g-C_3N_4/ZnO (100 mg) fiber. The reaction solution for the photoenzymatic reaction consisted of NAD^+ (1 mM), $[Cp^*Rh(bpy)H_2O]^{2+}$ (250 μM), α-ketoglutarate (5 mM), $(NH_4)_2SO_4$ (100 mM) and GDH (40 U) in 3 mL of phosphate buffer (100 mM, pH 7.0) containing 15 w% triethanolamine.

Photocurrent measurement: Photo-electrodes were prepared by drop casting of each samples (10 μg) on ITO glass (1 x 1 cm^2). Photocurrent responses were measured with prepared

photo-electrodes as working electrodes, a platinum wire as a counter electrode, Ag/AgCl reference electrode, and $NaSO_4$ (0.5 M) solution (as electrolyte) using WMPG 1000 potentiostat (WonATech, Korea). An applied potential for photo-electrodes against Ag/AgCl was set to 0.3 V.

Electrochemical analysis of $CaMn_2O_4$: Cyclic voltammetry (CV) was conducted using WMPG 1000 potentiostat (WonATech, Korea) with $CaMn_2O_4$ samples-Nafion (40 µg in 20 µL) deposited on glassy carbon electrode as a working electrode, a platinum wire as a counter electrode, and an Ag/AgCl reference electrode. The electrochemical reaction was performed in an O_2 saturated sodium phosphate solution (100 mM, pH 7.0) at room temperature with a scan rate of 50 mV s^{-1}.

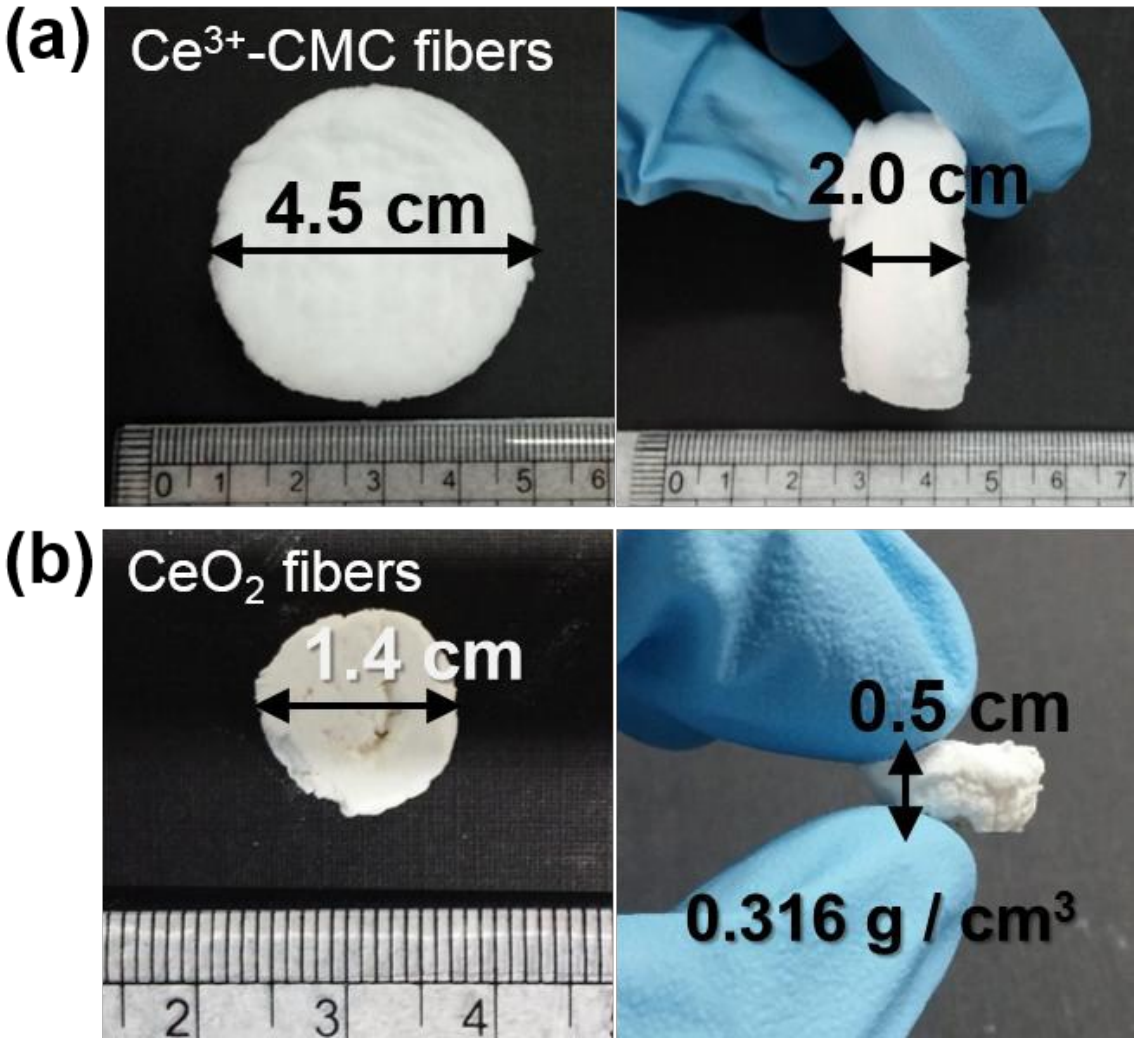

Figure S1. Photographs of Ce^{3+}-CMC fibers and free-standing CeO_2 synthesized from Ce^{3+}-CMC fibers.

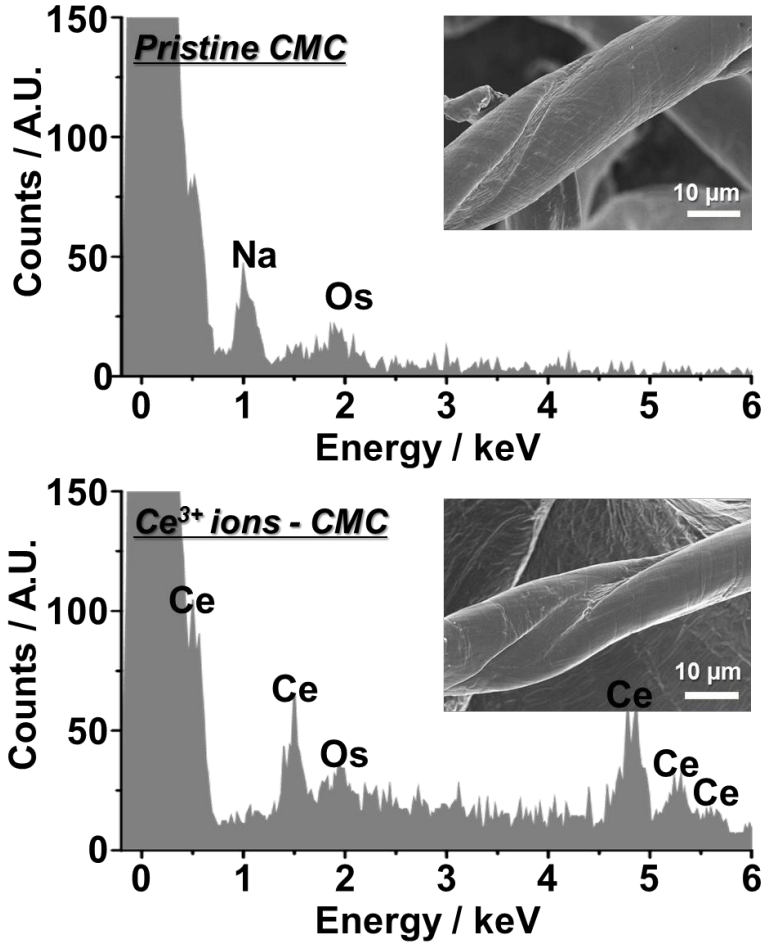

Figure S2. Surface analysis by EDX demonstrates that metal ions in the CMC fibers.

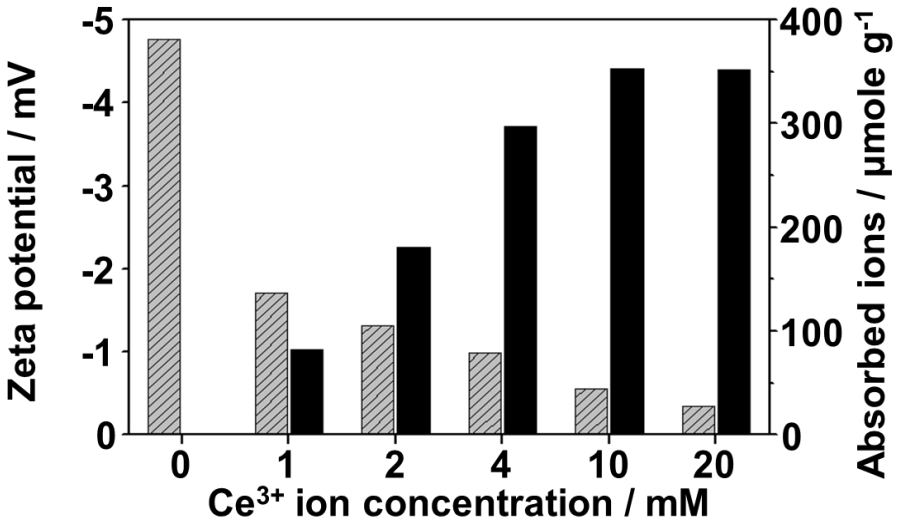

Figure S3. Zeta potential analysis of Ce^{3+} ion-adopted CMC fibers with the measured amount of Ce^{3+} ions in CM-cellulose.

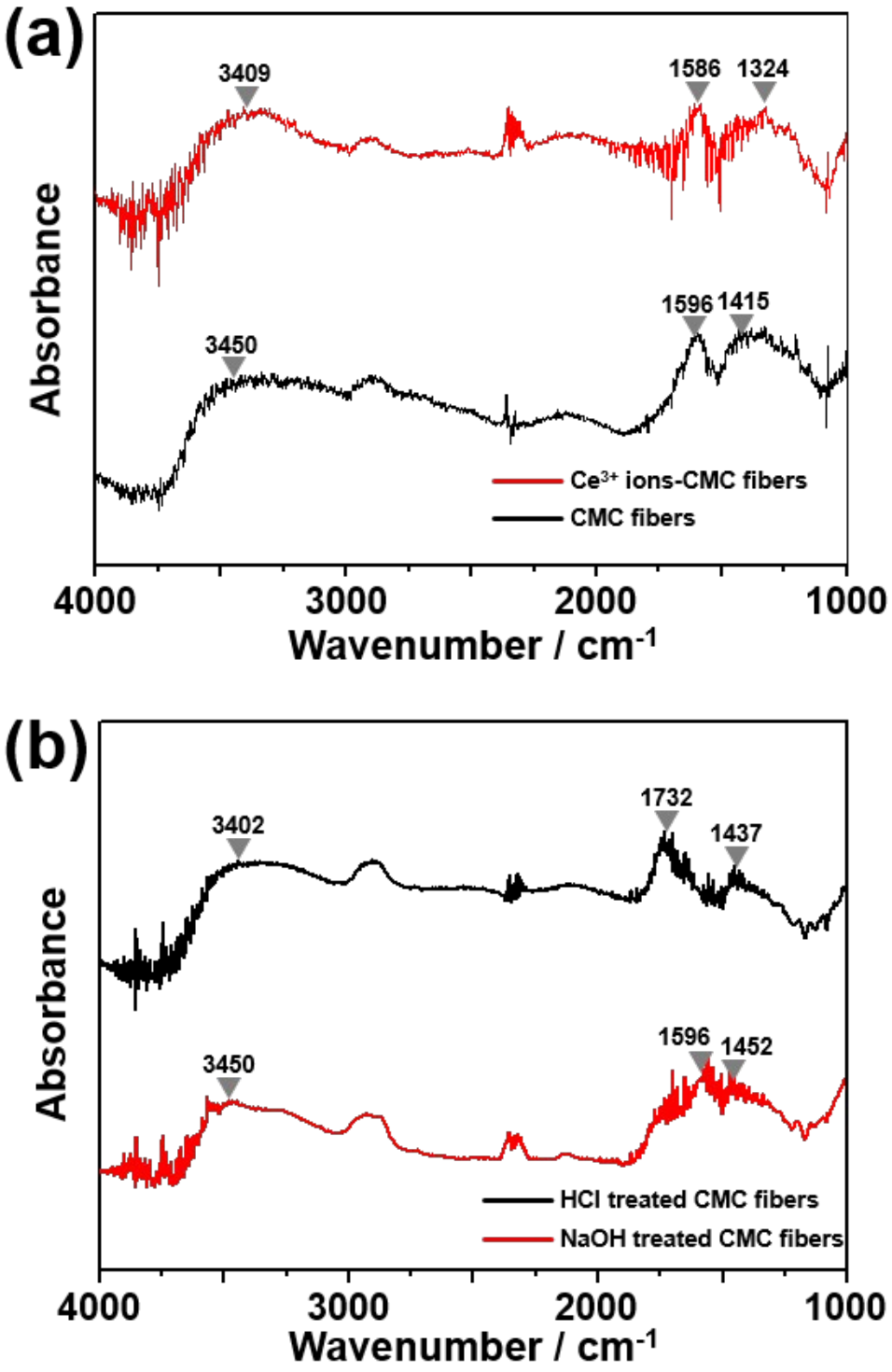

Figure S4. (a) FT-IR spectra of pristine CMC fibers and Ce^{3+}-CMC fibers. FT-IR absorption peaks corresponding to the stretching vibration modes of hydroxyl groups (~3400 cm^{-1}) and carboxyl groups (~1400 cm^{-1}). (b) FT-IR spectra of HCl (acid) and NaOH (basic) treated CMC fibers.

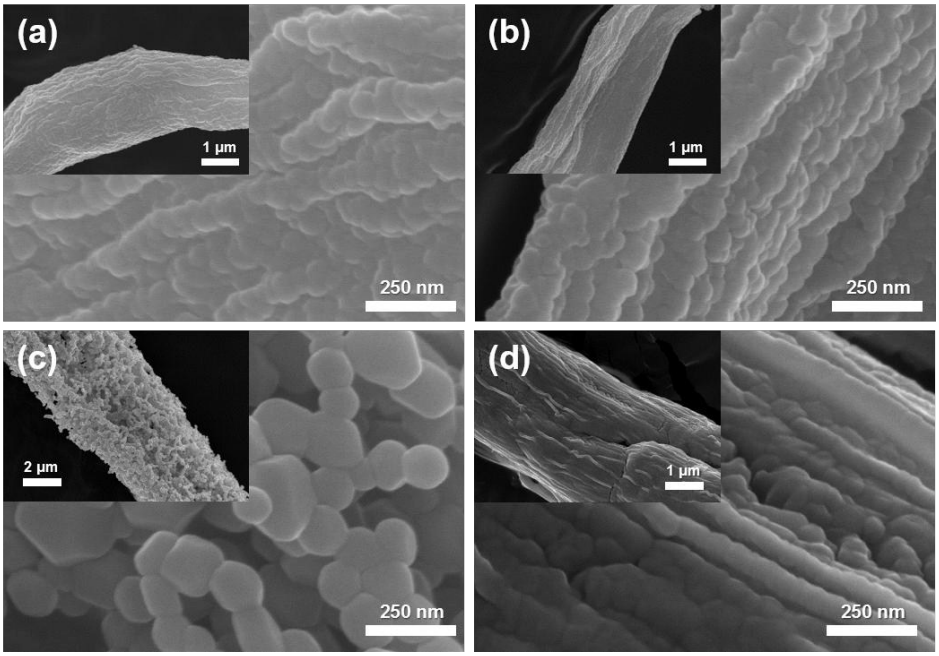

Figure S5. SEM images of CeO_2 fibers synthesized with different conditions [(a) 1 and (b) 4 mM of $CeCl_3$ solution and calcination temperature of 800 ℃ with HCl treated CMC, (b) 1 and (c) 4 mM of $CeCl_3$ solution and calcination temperature of 800 ℃ with NaOH treated CMC].

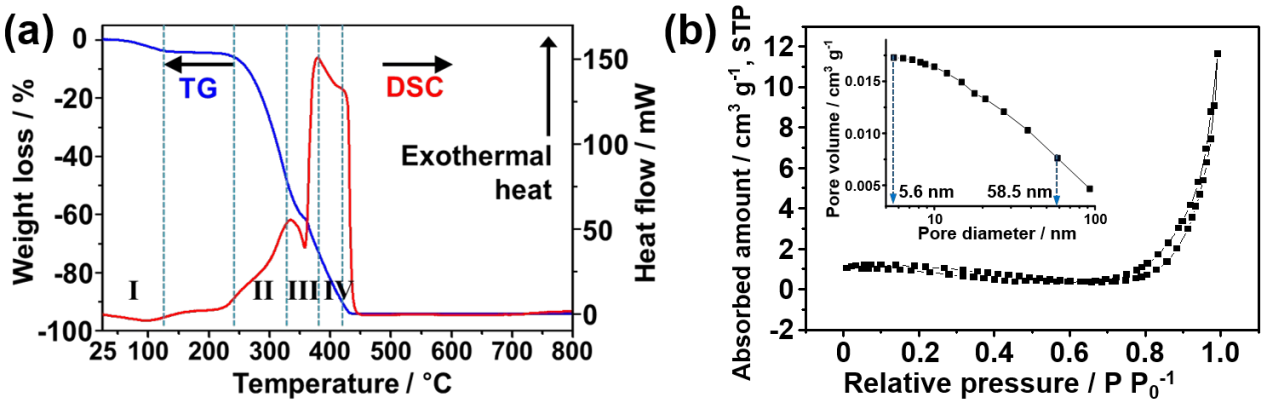

Figure S6. (a) Thermogravimetric analysis (TGA) and differential scanning calorimetry (DSC) curves of Ce^{3+}-adopted CMC fibers [(I) evaporation of water; (II) decomposition of cellulose fiber; (III) formation of CeO_2 phase; (IV) burn out of carbon backbone]. (b) Nitrogen adsorption-desorption isotherms and Barrett-Joyner-Halenda (BJH) pore size distribution (inset) of CeO_2 fibers.

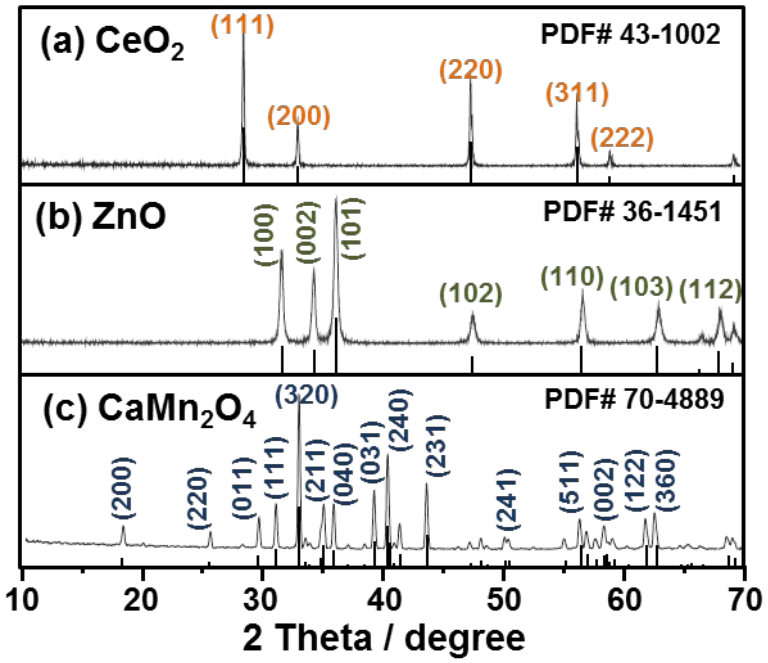

Figure S7. XRD spectra of the (a) CeO_2, (b) ZnO, and (c) $CaMn_2O_4$ fibers.

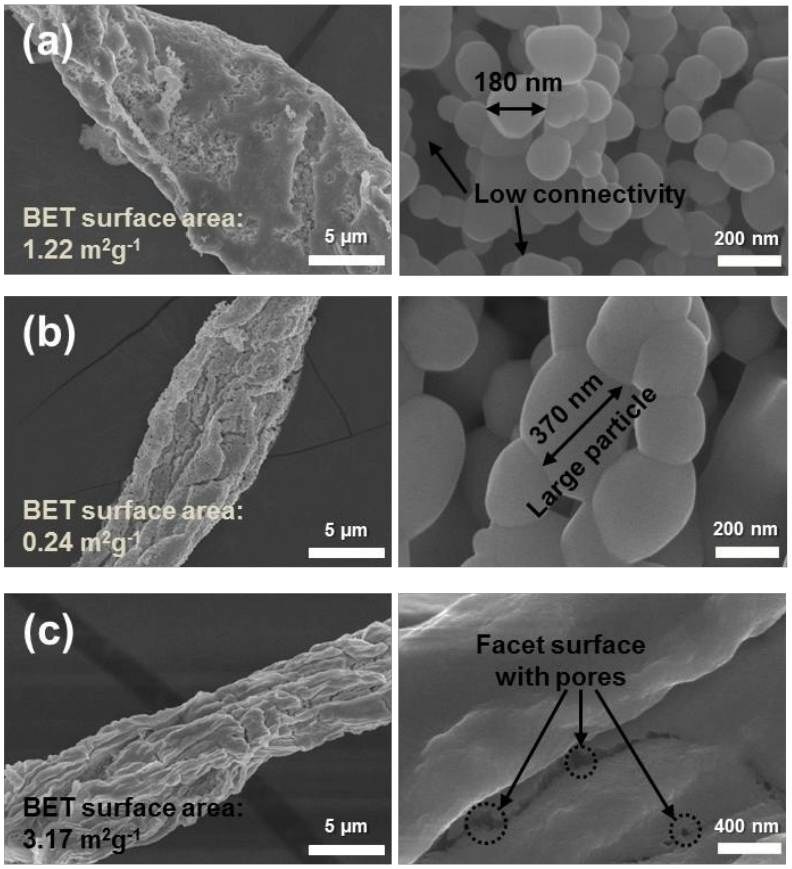

Figure S8. SEM images of CeO_2 fibers synthesized with different conditions [(a) 1 mM of $CeCl_3$ solution and calcination temperature of 800 ℃, (b) 4 mM of $CeCl_3$ solution and calcination temperature of 1000 ℃, and (c) 20 mM $CeCl_3$ solution with 800 ℃ calcination temperature].

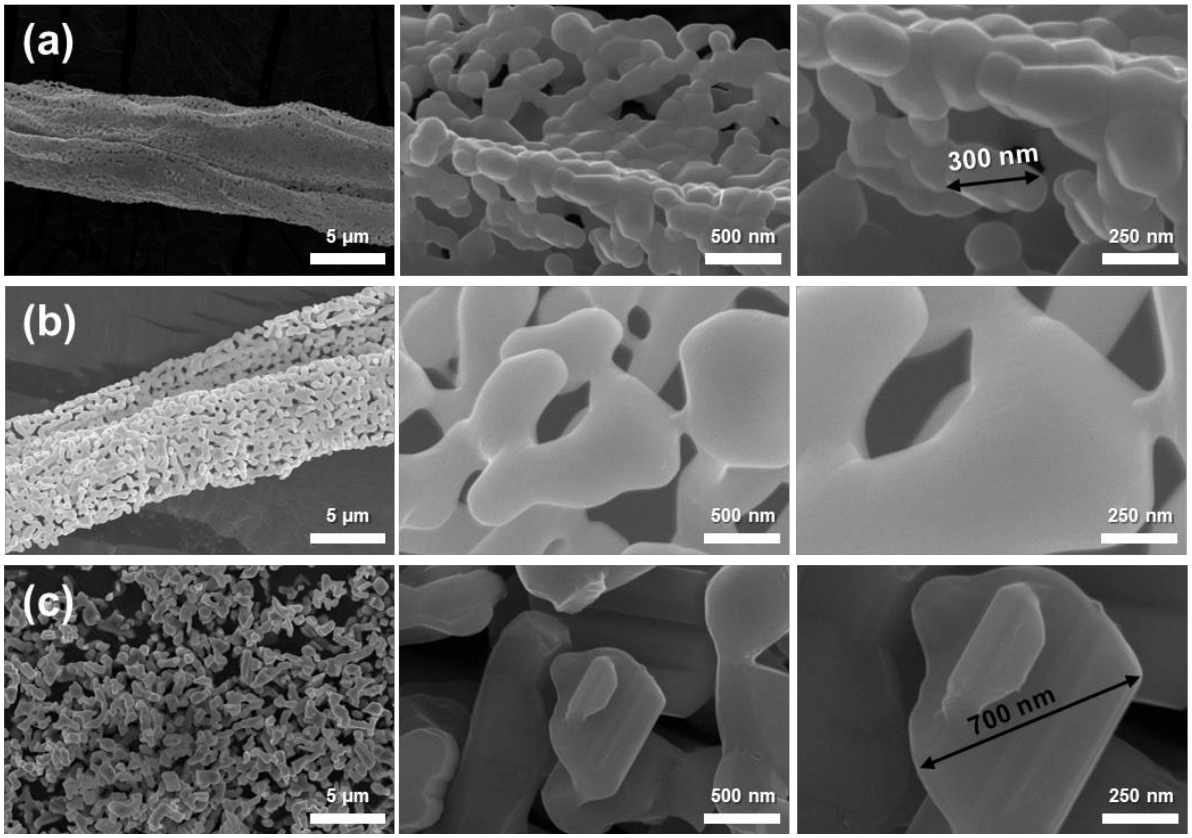

Figure S9. SEM images of $CaMn_2O_4$ synthesized with different amount of CM-cellulose; (a) 0.5 g, (b) 4 g, and (c) 6 g under identical experimental condition of precursor concentration and calcination temperature [1 mmole of $Ca(NO)_3 \cdot 4H_2O$ and 2.5 mmole of $Mn(NO)_3 \cdot 4H_2O$ in 40 ml of deionized water and calcination temperature of 1000 ℃ under the air].

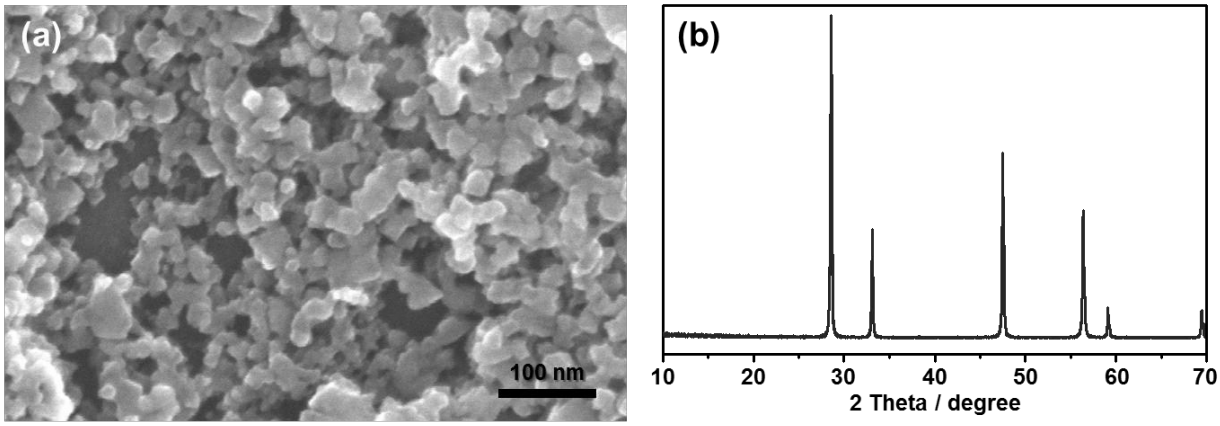

Figure S10. (a) SEM image of CeO_2 nanoparticles (purchased from Sigma-Aldrich Co., < 25 nm). (b) XRD spectrum showing the corresponding X-ray diffraction pattern of crystalline CeO_2.

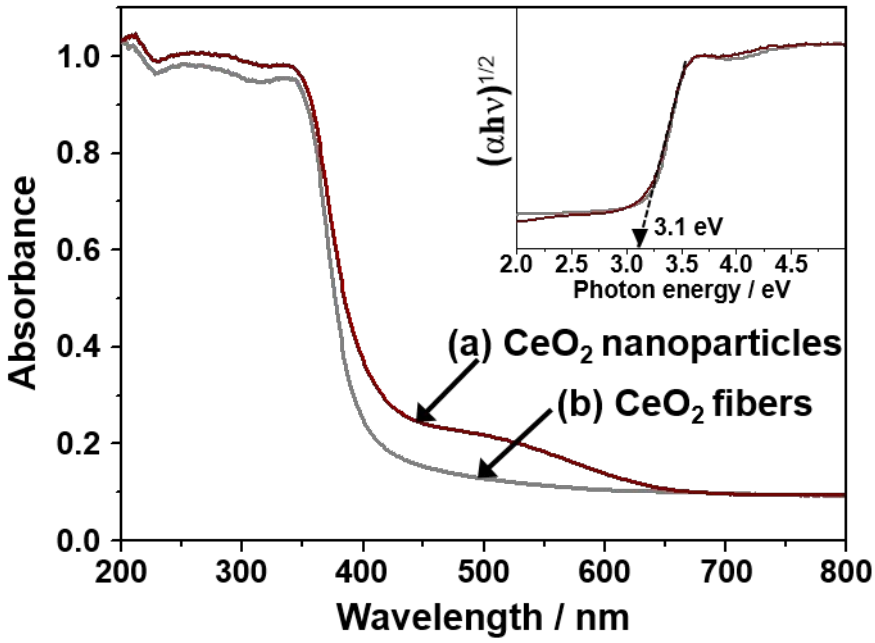

Figure S11. UV-visible absorbance spectra of (a) CeO_2 nanoparticles and (b) CeO_2 fibers synthesized using CMC. The inset spectra shows the relationship between the transformed Kubelka-Munk function versus photon energy for CeO_2 samples.

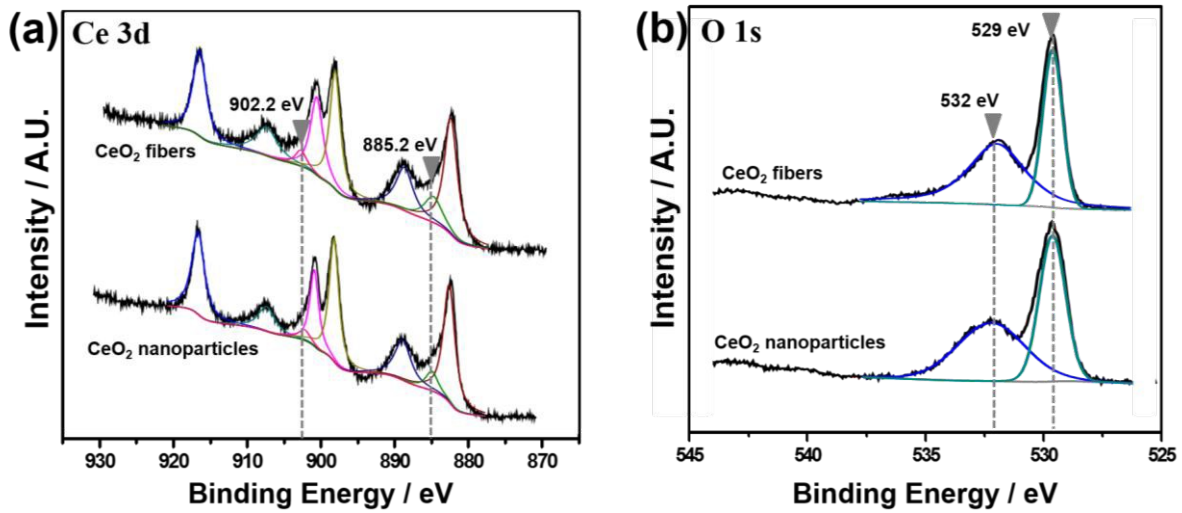

Figure S12. XPS spectra of CeO_2 fibers (synthesized with 4 mM of $CeCl_3$ solution and calcination temperature of 800 ℃), and CeO_2 nanoparticles (< 25 nm, purchased from Sigma Aldrich): (A) Ce 3d, and (B) O1s. The concentrations of Ce^{3+} ions on the surface of CeO_2 fibers and CeO_2 nanoparticles were calculated as 10.4% and 6.8%, respectively.

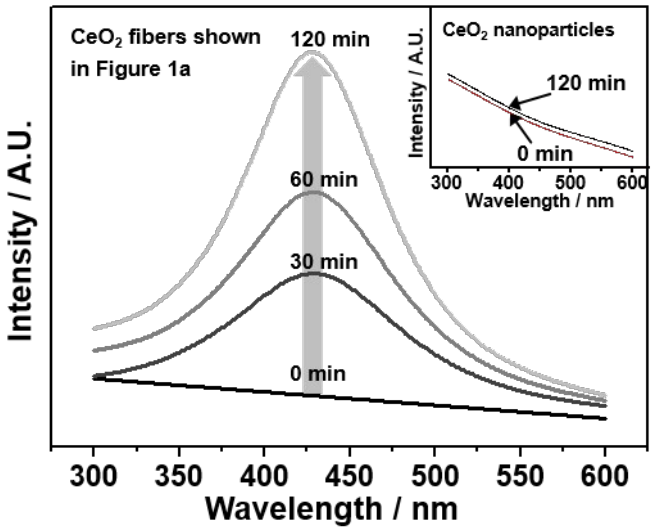

Figure S13. Fluorescence spectra of 2-hydroxyl terephthalate (TA-OH$^{\cdot}$) produced by MB and CeO_2 fibers (shown in Figure 1a) during photocatalytic reaction. In the case of CeO_2 nanoparticles, TA-OH$^{\cdot}$ was not generated (inset).

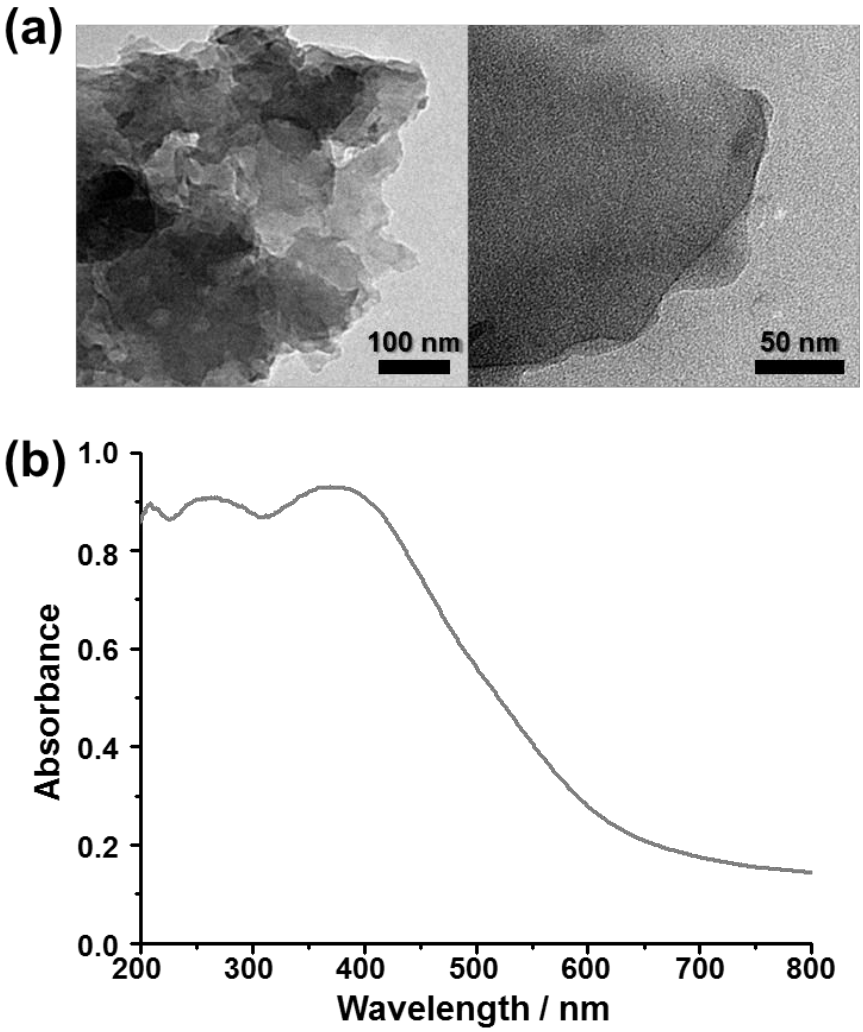

Figure S14. Characterizations of prepared g-C_3N_4 powder using TEM and UV-visible spectrophotometer. (a) TEM images of g-C_3N_4 powder exhibit a sheet-like two dimensional sheet-like structures in different magnifications. (b) UV-visible spectrum of g-C_3N_4 powder shows the strong absorption band in the range of 400-600 nm.

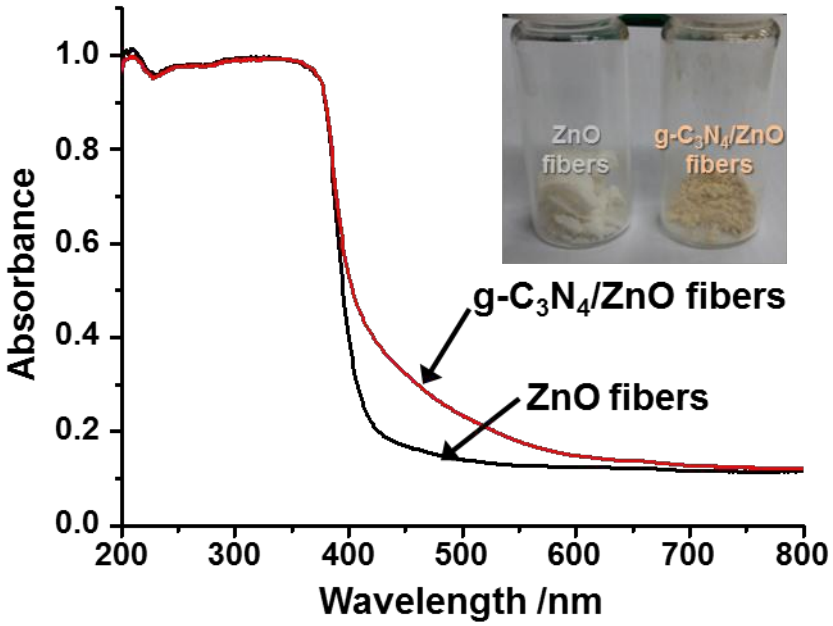

Figure S15. DRS spectra of ZnO fibers and g-C_3N_4/ZnO fibers, and a photograph of ZnO fibers and g-C_3N_4/ZnO fibers (inset). ZnO fiber had no absorbance in the visible light range. [black solid line] After hybridization with g-C_3N_4, g-C_3N_4/ZnO fibers exhibit increased absorbance in the range of 400-600 nm. [red solid line]

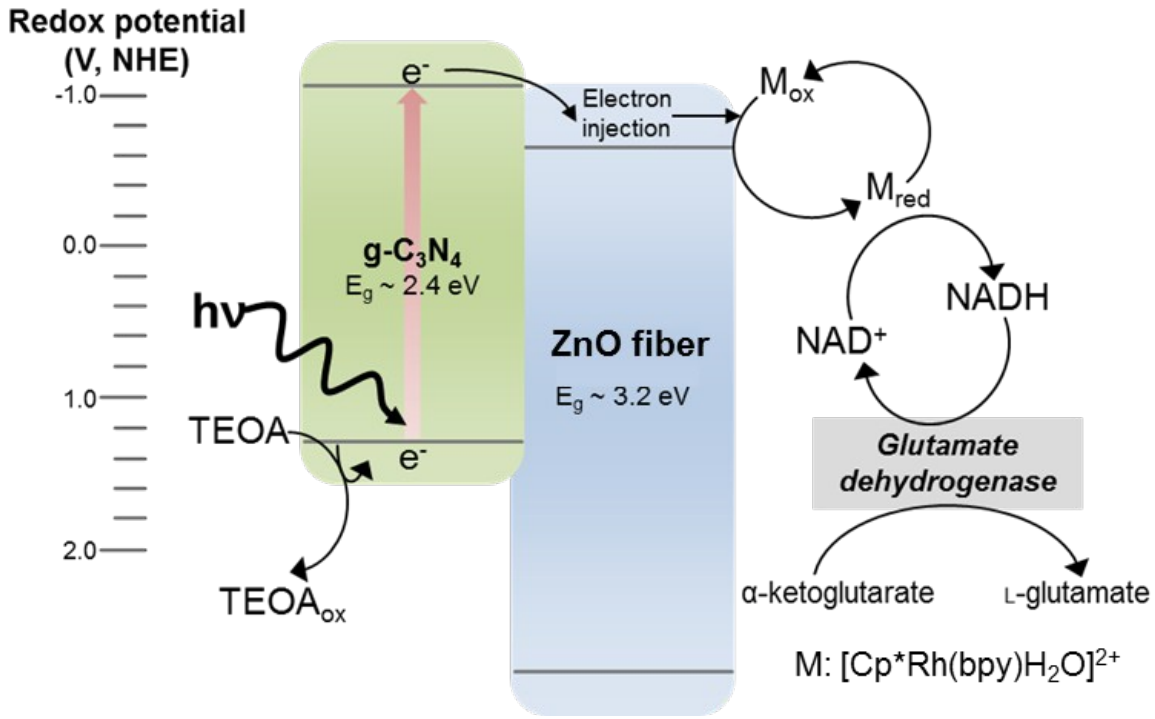

Figure S16. Proposed mechanism of an electron transfer between g-C_3N_4 and ZnO fiber, and photochemical NADH regeneration with gC_3N_4/ZnO fiber through an electron mediator (**M** = $[Cp^*Rh(bpy)H_2O]^{2+}$].

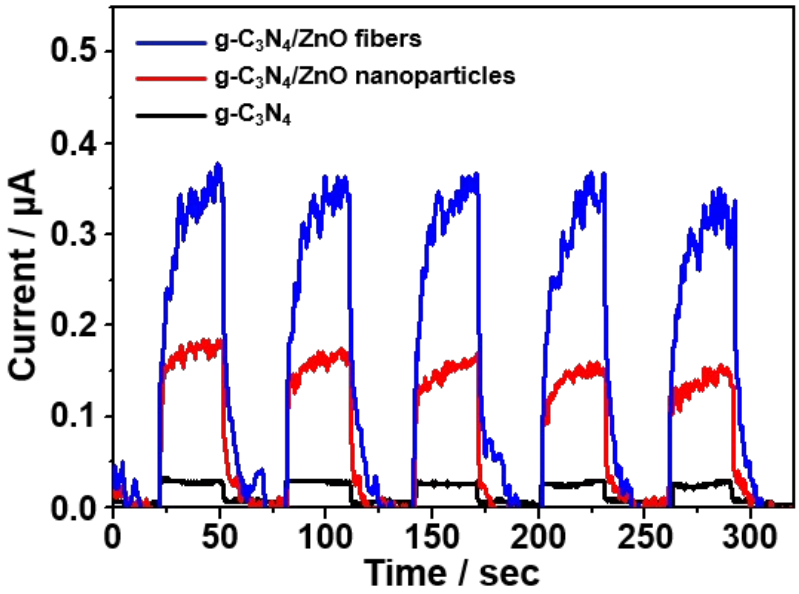

Figure S17. Photocurrent response for bare g-C_3N_4, g-C_3N_4/ZnO nanoparticles, and g-C_3N_4/ZnO fibers under visible light irradiation.

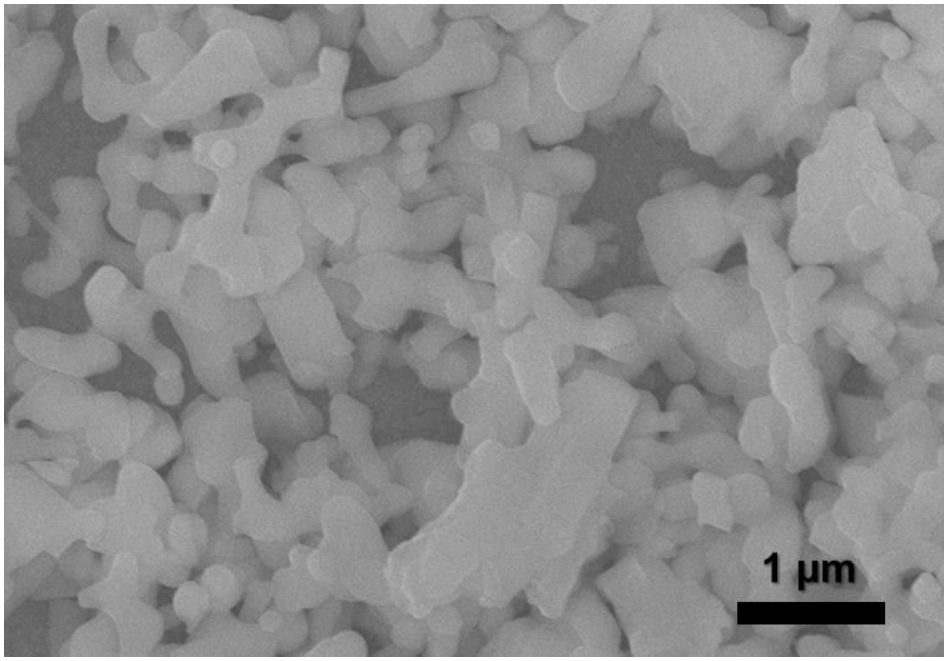

Figure S18. SEM image of bulk $CaMn_2O_4$ synthesized using conventional hydrothermal method.

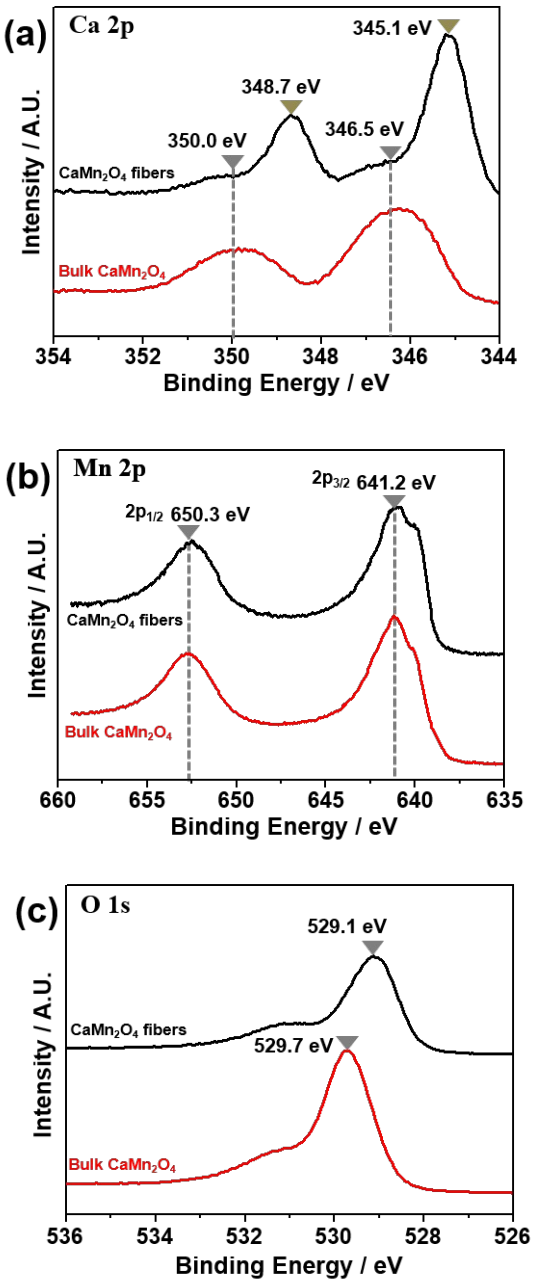

Figure S19. XPS spectra of Ca 2p, Mn 2p, and O 1s of $CaMn_2O_4$ fibers and Bulk $CaMn_2O_4$.